ACS OMEGA

Open Access

http://pubs.acs.org/journal/acsodf

Article

2D Hybrid Nanocomposite Materials (h-BN/G/MoS_2) as a High-Performance Supercapacitor Electrode

Chandra Sekhar Bongu, Muhammad Arsalan, and Edreese H. Alsharaeh*

Cite This: *ACS Omega* 2024, 9, 15294−15303

Read Online

ACCESS | Metrics & More | Article Recommendations | Supporting Information

ABSTRACT: The nanocomposites of hexagonal boron nitride, molybdenum disulfide, and graphene (h-BN/G/MoS_2) are promising energy storage materials. The originality of the current work is the first-ever synthesis of 2D-layered ternary nanocomposites of boron nitrate, graphene, and molybdenum disulfide (h-BN/G/MoS_2) using ball milling and the sonication method and the investigation of their applicability for supercapacitor applications. The morphological investigation confirms the well-dispersed composite material production, and the ternary composite appears to be made of h-BN and MoS_2 wrapping graphene. The electrochemical characterization of the prepared samples is evaluated by cyclic voltammetry and galvanostatic charge/discharge tests. With a high specific capacitance of 392 F g^{-1} at a current density of 1 A g^{-1} and an outstanding cycling stability with around 96.4% capacitance retention after 10,000 cycles, the ideal 5% BN_G@MoS_2_90@10 composite demonstrates exceptional capabilities. Furthermore, a symmetric supercapacitor (5% BN_G@MoS_2_90@10 composite) exhibits a 94.1% capacitance retention rate even after 10,000 cycles, an energy density of 16.4 W h kg^{-1}, and a power density of 501 W kg^{-1}. The findings show that the preparation procedure is safe for the environment, manageable, and suitable for mass production, which is crucial for advancing the electrode materials used in supercapacitors.

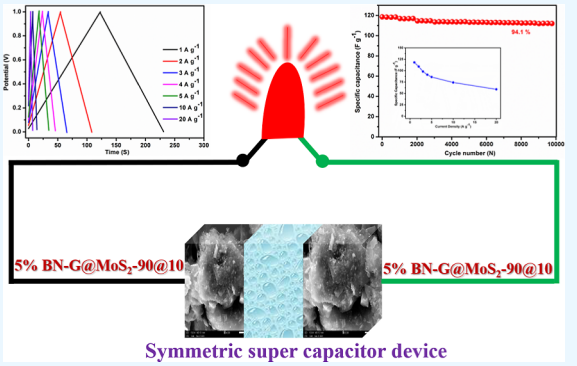

1. INTRODUCTION

Numerous types of electrochemical energy systems have been developed to meet the rapidly expanding demand for renewable energy in the human society.[1] Lithium-ion batteries, supercapacitors, aqueous zinc-ion batteries, and fuel cells are a few typical examples. Among them, supercapacitor (SC) is a desirable energy storage device because of its high-power density, quick charge/discharge, and long cycle life.[2,3] SCs can be divided into electrical double-layer capacitors (EDLCs) and pseudocapacitors based on the energy storage mechanism.[4] While pseudocapacitors primarily use electroactive conducting polymers or transition-metal oxides as electrode materials, EDLCs are often constructed of carbon materials or carbon-based hybrid materials with high surface areas and acceptable pore sizes.[5−10]

In recent years, two-dimensional (2D) transition-metal dichalcogenides have received significant attention due to their unique graphite-like layered structure.[11,12] These materials' chemical, electrical, thermal, and mechanical characteristics open up a wide range of application.[13,14] Molybdenum disulfide (MoS_2), in particular, provides important indications in acting as a satisfactory electrode material that it has a place in supercapacitor applications among various binary chalcogenides, such as disulfides, diselenides, and ditellurides of transitional-metal elements with intriguing sheet-like structure.[15−17] Its enormous surface area and hexagonal-like structure make it a desirable material for use in supercapacitors.[18] To date, some reports have been concentrated on the supercapacitor characteristics of pure MoS_2 with various morphologies.[19,20] For instance, Huang et al. reported that MoS_2 nanosheets as electrode materials had a specific capacitance retention of 85.1% after 500 cycles and a capacitance of up to 129.2 F g^{-1} at 1 A g^{-1}.[21] Wang et al. created flower-like MoS_2 that, when used as electrode materials for electrochemical capacitors, demonstrated a specific capacitance of 168 F g^{-1} at 1 A g^{-1}.[22]

To the best of our knowledge, pure MoS_2 utilized as an electrode material alone still has very limited energy storage applications due to its interlayer van der Waals interactions and high surface energy and nanosheets which can rearrange, leading to poor electronic conductivity and significant volume change of the material throughout the charge/discharge process.[23−27] Eventually, the SCs' cycling abilities substantially deteriorate. Therefore, to fill the gap in increasing electrical

Received: December 11, 2023
Revised: February 8, 2024
Accepted: March 12, 2024
Published: March 22, 2024

conductivity and capacitance performance, several researchers have turned to combining MoS_2 with other conducting materials.[15,16,28−34] Due to its exceptional electrical conductivity, enormous surface area, high mechanical resilience, and excellent chemical stability, graphene, a 2D layered material with zero band gap, has been widely used in electrochemical capacitors.[35−38] Therefore, the composites of MoS_2 and graphene would possess excellent electrochemical properties compared to that of pure MoS_2 and graphene for the application of supercapacitors.[15,39,40]

An example of a 2D material was hexagonal boron nitride (h-BN), which was comparable to graphene and molybdenum disulfide (MoS_2). The use of h-BN as a polymer filler in a variety of applications, from electrical to biomedical, has been established. It has good thermal stability, high hydrophobicity, and high thermal conductivity.[41,42] The electronic industry prefers using h-BN as a filler material because of its ability to absorb moisture, dielectric constant, and thermal expansion coefficient.[43] Application of h-BN, which includes electrolytes and electrodes, to energy storage devices like supercapacitors may present a favorable opportunity and advance the area.[44−47] The h-BN act as a filler for the graphene and MoS_2 from the interlayer interactions and agglomeration,[42] therefore, the combination of MoS_2 and graphene with h-BN would definitely be a promising candidate for next-generation supercapacitors.

In this paper, we demonstrate that nanocomposites of h-BN with MoS_2 and graphene would be an excellent candidate for use as a supercapacitor. We employed a ball milling method for the preparation of MoS_2 and graphene composition. Following this, we have followed the sonication process for h-BN with the graphene/MoS_2 composite to get the final ternary composite (h-BN/graphene/MoS_2). In the three composites, the optimal composite (5% BN_G@MoS_2_90@10) exhibits a high specific capacitance of 392 F g^{-1} when tested at a current density of 1 A g^{-1} for 10, 000 cycles, and the retention rate was 96.4%. Inspired by these results, a supercapacitor was fabricated using two identical (symmetric supercapacitor) 5% BN_G@MoS_2_90@10 electrodes. The assembled device yielded 94.1% of capacitance retention rate even after 10,000 cycles, an energy density of 16.4 Wh kg^{-1}, and a power density of 501 W kg^{-1}. These outstanding behaviors are attributed to the ternary nanocomposite of graphene, MoS_2, and h-BN.

2. EXPERIMENTAL SECTION

2.1. Materials. Molybdenum(IV) sulfide (∼98%) and h-BN (∼98%) were purchased from Graphene supermarket. Graphene powder (99.9999%) was purchased from XG sciences. Carbon black (50% compressed) and poly(vinylidene fluoride) powder were purchased from MTI Corporation. *N*-Methyl-2-pyrrolidone (∼99.5%) was purchased from Merck. For cleaning, acetone (≥99.0%) and ethanol (≥99.0%) were purchased from Sigma-Aldrich.

2.2. Material Preparation. *2.2.1. Preparation h-BN/Graphene/MoS_2 Composites.* In the first step, MoS_2/graphene (50:50, 10:90, and 90:10) nanocomposites were synthesized via the ball milling and sonication process by using graphene and MoS_2 as starting materials. The graphene powder and MoS_2 powder were ground for 30 min and ball milled with different ratios (50:50, 10:90, and 90:10 ratios) [powder weight ratio with balls to material was 4:1 with the 1060 rotational speed (rpm)] for 45 min by using SPEX samplePrep P instrument [model number 8000 M MIXER/MILL using two different sizes of the balls (four balls with 6.3 mm and two balls with 12.5 mm prepared with stainless steel)]. To get better uniformity, the above ratio powers were dispersed in ethanol (25 mL) by using ultrasonication (250 W 20 kHz, model VWR Ultrasonic cleaner USC THD instrument) for 60 min at room temperature. The yield of the MoS_2@graphene nanohybrids was dried in the vacuumed furnace at 100 °C for 6 h. Afterward, MoS_2 with graphene composites (50:50, 10:90, and 90:10 ratios) was ball milled with 5 wt % of BN for 45 min and subsequently ultrasonicated for 60 min to get better uniformity. The final products of 5% BN_G@MoS_2_50@50, 5% BN_G@MoS_2_90@10, and 5% BN_G@MoS_2_10@90 were obtained by ultrasonicated material dried in the vacuumed furnace at 100 °C for 6 h.

3. CHARACTERIZATION

3.1. Physicochemical Characterization. A Bruker D8 Advance X-ray diffractometer with a scanning range of 10−70° in 2θ and Cu Ka radiation (λ = 1.5406) was used to acquire the X-Ray diffraction (XRD) data. Surface morphology of synthesized material was investigated using Gemini scanning electron microscopy (SEM), transmission electron microscopy (TEM), and high-resolution transmission electron microscopy (HRTEM) by using FEI Quanta 200 and TEM, JEOL2100 Instruments. For sample preparation, the powder composite sample was dispersed in an ethanol−water mixture by 20 min ultrasonication, followed by drop-casting onto a fresh lacey carbon copper grid. Raman spectra of the samples were collected using WITec Apyron Raman microscope equipment and a 532 nm solid-state laser as the excitation source. X-ray photoelectron spectroscopy (JEOL JPS-9030) was utilized to study the elemental composition and oxidation states of elements by passing an energy of 20 eV.

3.2. Electrochemical Characterization. The electrochemical performance tests including cyclic voltammetry (CV), galvanostatic current charge−discharge (GCD), and electrochemical impedance spectroscopy (EIS) methods (AC voltage of 5 mV) in the three-electrode or two-electrode system were implemented by using a BioLogic SP-300 Modular electrochemical workstation. The 5% BN-G@MoS_2-10@90, 5% BN-G@MoS_2-50@50, and 5% BN-G@MoS_2-90@10 were used to fabricate the working electrodes. The composite samples (BN-G@MoS_2) were mixed with carbon black (Super-P) and poly(vinyl difluoride) (PVDF) in a weight ratio of 85:10:5 and coated on the nickel foam. The mass loading of the three-electrode materials on the nickel foam (15 mm) was 1.0−1.5 mg. The working electrodes were obtained after drying at 60 °C overnight in a vacuum oven. The electrochemical tests of the individual electrodes were performed using 6 M aqueous KOH solution as the electrolyte in a three-electrode cell in which platinum foil and Ag/AgCl were used as counter and reference electrodes, respectively. The symmetric supercapacitors performed using the 5% BN-G@MoS_2-90@10 electrode as both the cathode and anode in a two-electrode system and the separator was Whatman filter paper. All measurements were taken at room temperature.

For three-electrode cells, the capacitance was calculated using the charge integrated from GCD curves, according to the following formula

$$C_s = \frac{I\Delta t_d}{m\Delta V} \quad (1)$$

https://doi.org/10.1021/acsomega.3c09877
ACS Omega 2024, 9, 15294−15303

where I is the discharge current (A), Δt is the discharge time (s), m is the mass of the active material (g), and ΔV is the discharge potential window (V).

The energy density (E, W h kg^{-1}) at different power densities (P, W kg^{-1}) of the supercapacitor cell could be calculated from the GCD curves at different current densities according to eqs 2 and 3

$$E = \frac{0.5 \times C_{CD} \times (\Delta V)^2}{3.6} \quad (2)$$

$$P = \frac{E}{\Delta t} \quad (3)$$

where ΔV is the potential window of discharge (V) and Δt is the discharge time (s).

4. RESULTS AND DISCUSSION

4.1. Physicochemical Characterization. The crystal structure and phase information on the samples (5% BN-G@MoS_2-50@50, 5% BN-G@MoS_2-10@90, and 5% BN-G@MoS_2-90@10) were obtained by X-ray diffraction spectroscopy, as shown in Figure 1. The diffraction peak located at 26.4°

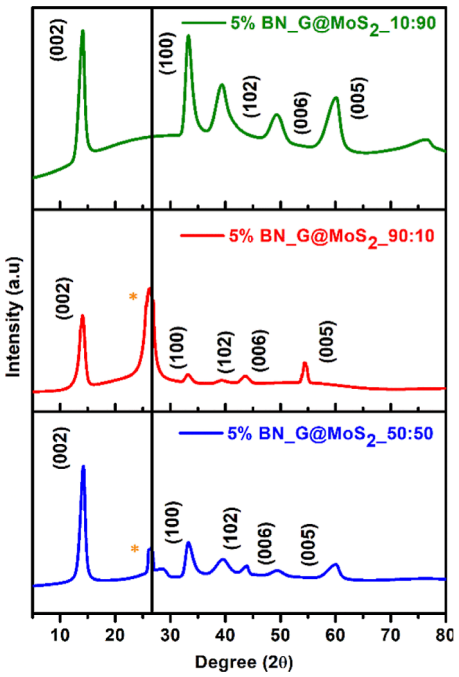

Figure 1. XRD patterns of the 5% h-BN/G/MoS_2 nanocomposites (1:9, 5:5, and 9:1).

in the 5% BN-G@MoS_2-50@50 and 5% BN-G@MoS_2-90@10 is corresponded to the (002) crystallographic plane of graphene, and this plane disappeared in the pattern of 5% BN-G@MoS_2-10@90 nanocomposites, revealing that graphene is insufficient in the composition. The diffraction peaks located at 14.1, 33.1, 39.4, 43.8, and 54.4° correspond to the (002), (100), (102), (006), and (110) crystallographic planes of MoS_2, respectively, which are in good agreement with the standard card of JCPDS no. 37-1492.[48,49] However, 5% BN-G@MoS_2-90@10 exhibits slightly broader peaks, thus indicating nanocrystalline product formation, aided by the increased graphene content. On the other hand, 5% BN-G@MoS_2-50@50 shows a diminished (100) peak at 2θ = 26.4° and slightly enhanced intensity for peaks located at 2θ = 14.1°, which is considered as a MoS_2 dominating the overall composition. As a result, the XRD of 5% BN-G@MoS_2-90@10 exhibits strong and intense peaks at 2θ = 14.1° and 2θ = 26.4° corresponding to MoS_2 and graphene would be beneficial for an easy charge transport for the application in supercapacitors.

Further analysis of the interplay between BN, MoS_2, and G during the sonication and ball-milling process was done using Raman spectroscopy, as shown in Figure 2. The characteristic

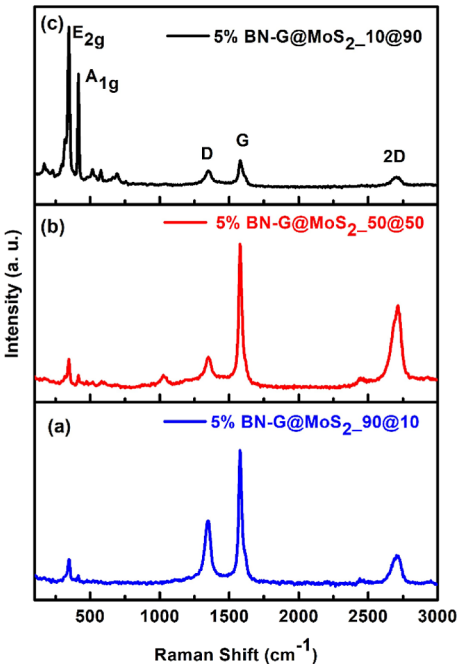

Figure 2. Raman spectra of (a) 5% BN-G@MoS_2-90@10, (b) 5% BN-G@MoS_2-50@50, and (c) 5% BN-G@MoS_2-10@90 samples.

Raman peaks of composites detected at 350, 423, 1348, 1585, and 2703 cm^{-1} are ascribed to the in-plane $^1E_{2g}$, out-of-plane A_{1g} vibrational modes, D band (disorderly defect structure), G band (sp^2-bonded carbon atoms), and 2D mode, respectively.[50,51] The peaks at 350 and 423 cm^{-1} are Mo−S bands corresponding to in-plane $^1E_{2g}$ and out-of-plane A_{1g} vibrational modes for MoS_2. In the case of the 5% BN-G@MoS_2-90@10 composite with the maximum amount of MoS_2, the in-plane $^1E_{2g}$ and out-of-plane A_{1g} vibrational modes of MoS_2 are clearly visible with small peaks of graphene and BN. For the 5% BN-G@MoS_2-50@50 composite with an equal amount of graphene and MoS_2, the sharp peaks attributed to the D and G bands contributed by h-BN and graphene and the $^1E_{2g}$ and A_{1g} vibrational mode intensity was very small. However, in the case of 5% BN-G@MoS_2-90@10, the least amount of MoS_2, the $^1E_{2g}$ and A_{1g} vibrational modes showed less intensity, and D and G bands are of high intensity. The crystal size of the composites was calculated by using full width at half-maximum of the composites, and 5% BN-G@MoS_2-90@10 shows small size compared to the 5% BN-G@MoS_2-50@50 and 5% BN-G@MoS_2-10@90 composites. Raman analysis clearly explained that MoS_2 embedded in the graphene and BN sheets.

SEM was used to examine the morphologies and microstructures of the as-prepared (5% BN-G@MoS_2-50@50, 5% BN-G@MoS_2-10@90, and 5% BN-G@MoS_2-90@10) compo-

https://doi.org/10.1021/acsomega.3c09877
ACS Omega 2024, 9, 15294−15303

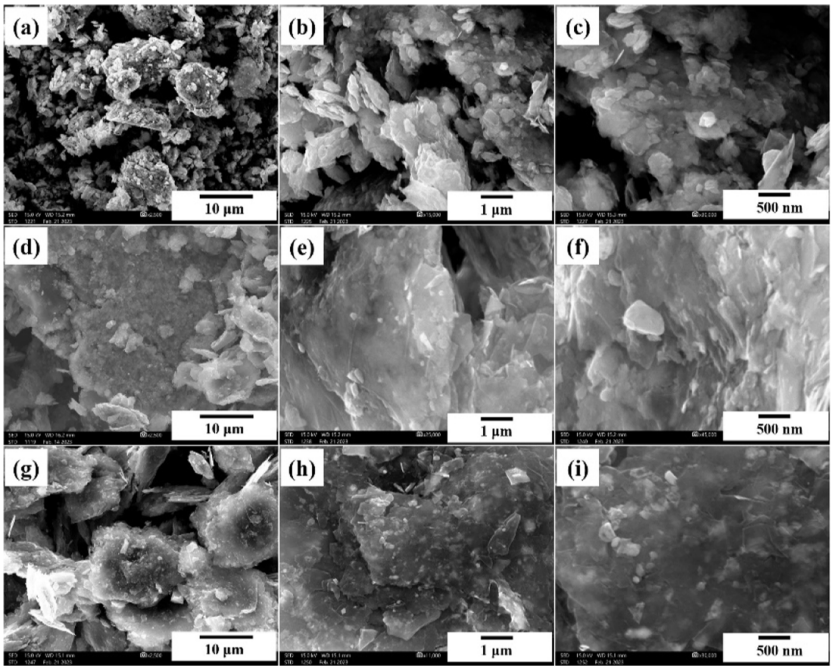

Figure 3. SEM images of the as-prepared 5% h-BN/G/MoS_2 nanocomposites. (a–c) 5% BN-G@MoS_2-10@90, (d–f) 5% BN-G@MoS_2-50@50, and (g–i) 5% BN-G@MoS_2-90@10.

site, as shown in Figure 3. Figure S1, elemental mapping study of the 5% BN-G@MoS_2-90@10 composite, shows compelling evidence of the homogeneous distribution of the elements C, O, Mo, S, B, and N. SEM images clearly suggest that the morphology of the compositions Is greatly influenced by the ratios of graphene and MoS_2. As shown in Figure 3a–c, the composition of 5% BN-G@MoS_2-10@90, the entire MoS_2 is not covered with a graphene substrate network and agglomerated with each other. Apart from that 5% BN-G@MoS_2-50@50 (Figure 3d–f) and 5% BN-G@MoS_2-90@10 (Figure 3g–i) composites are different; the graphene sheets are clearly visible with a sufficient amount which is in agreement with the findings from TEM and HRTEM (Figures 4 and S2). Figure 4 makes it evident that each individual MoS_2 particle has a carbon covering (gray color). The magnified view of Figure 4c,d demonstrates the existence of individual MoS_2 with a thin line of carbon coating to prevent aggregation and to constrain enable the inevitable volume increase. Especially, MoS_2 was uniformly dispersed and well decorated on the graphene sheet in the 5% BN-G@MoS_2-90@10 nanocomposite; the aggregation of the nanosheets was restrained in the composition. As shown in Figure S2a,b, both the HRTEM images reveal that MoS_2 and graphene overlap (parallel) each other with BN material, confirmed by the spacing of MoS_2 at 2.9 Å.[S2]

Elemental analysis and X-ray photoelectron spectroscopy (XPS) were also acquired to examine the as-prepared product's chemical composition and phase state of 5% BN-G@MoS_2-90@10. The XPS full survey spectrum of 5% BN-G@MoS_2-90@10 is shown in Figure S3a, where the presence of the elements Mo, S, B, N, C, and O is visible. Two distinct peaks, located at 229.4 and 233.3 eV in the high-resolution XPS spectra of MoS_2 5% BN-G@MoS_2-90@10 (Figure S3b), are indicative of the Mo^{4+} $3d_{5/2}$ and Mo^{4+} $3d_{3/2}$ components of the compound, respectively. Another minor peak at 226.6 eV is the S 2s of MoS_2, and other peaks are seen at 162.3 and 163.5 eV,

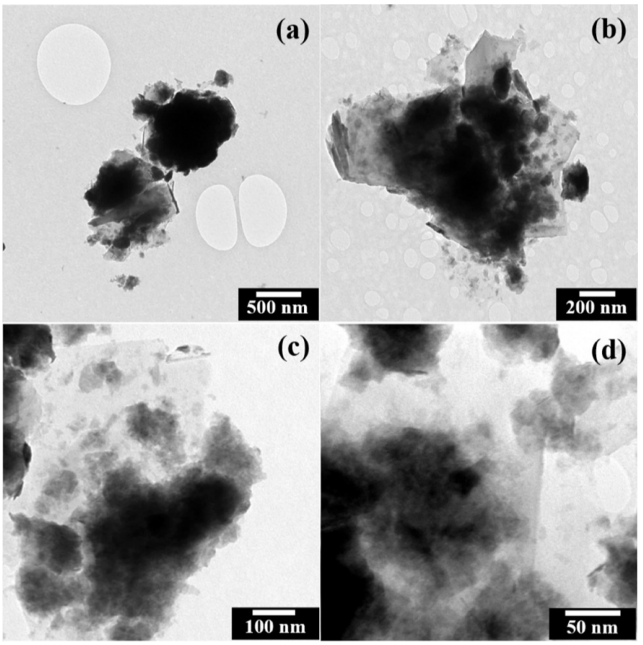

Figure 4. TEM images of (a–d) 5% BN-G@MoS_2-90@10 nanocomposite.

respectively, due to $S^{2-}2P_{3/2}$ and $S^{2-}2P_{1/2}$ (Figure S3c). The B–N peak at 190.78 eV and the N–B peak at 398.37 eV in Figure S3d and Figure S3e, respectively, are designated as the B 1s and N 1s spectra. These spectra arise from the BN of some boron and nitrogen atoms at the 5% BN-G@MoS_2-90@10 sample surface. The C 1s spectra in Figure S3f are identified as two distinct peaks with binding energies of 284.4 and 285.8 eV, attributed to sp^2-hybridized graphitic carbon C=C, C–C, and C=O configurations, respectively. This finding demonstrates that the ball milling approach successfully created the 5% BN-G@MoS_2-90@10 nanocomposite. Additionally, the

https://doi.org/10.1021/acsomega.3c09877
ACS Omega 2024, 9, 15294–15303

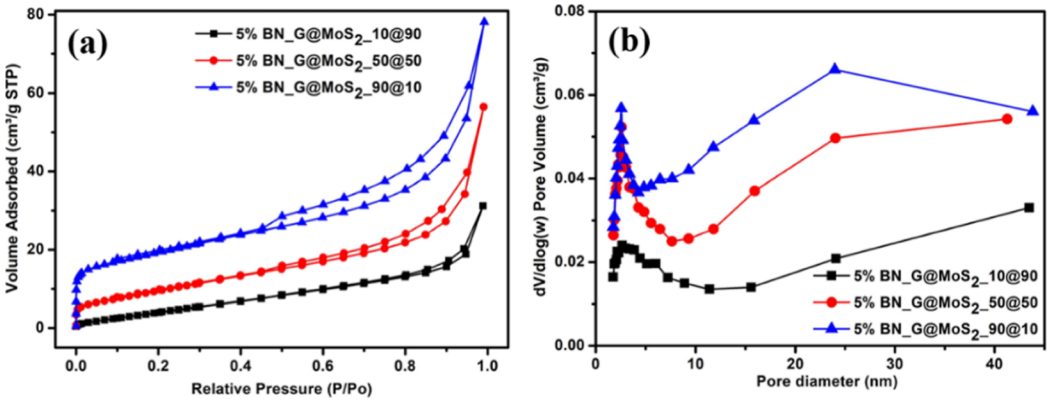

Figure 5. (a) Nitrogen adsorption/desorption isotherms and (b) the corresponding pore size distribution curves of 5% BN-G@MoS_2-10@90, 5% BN-G@MoS_2-50@50, and 5% BN-G@MoS_2-90@10.

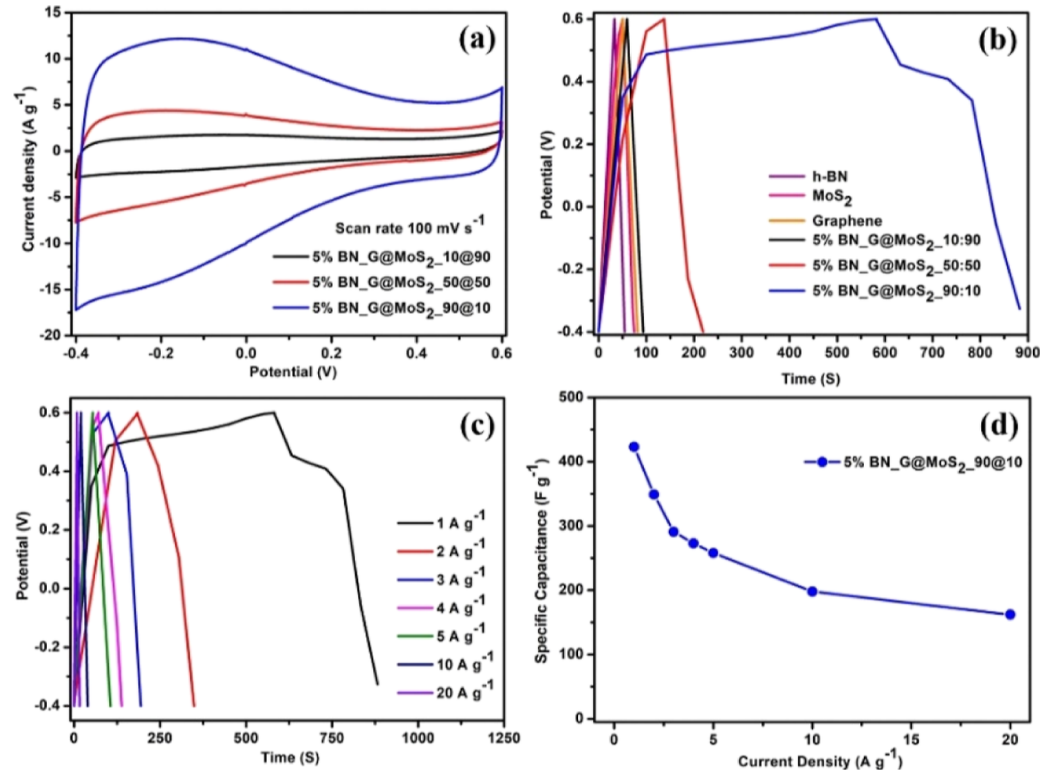

Figure 6. Electrochemical performances of 5% BN_G@MoS_2 nanocomposite (1:9, 5:5, and 9:1) electrodes in a three-electrode system: (a) CV curves at 100 mV s^{-1}. (b) GCD curves of h-BN, MoS_2, graphene, and 5% BN_G@MoS_2 nanocomposite (1:9, 5:5, and 9:1) at 1 A g^{-1}. (c) Charge/discharge profiles of 5% h-BN_G@MoS_2_90@10 at different current densities. (d) Specific capacitance of 5% h-BN_G@MoS_2_90@10 at different current densities.

nanocomposite contains certain oxygen groups that can potentially adsorb heavy metals through complexation.

The surface areas and porosities of the as-prepared 5% BN-G@MoS_2-10@90, 5% BN-G@MoS_2-50@50, and 5% BN-G@MoS_2-90@10 composite samples are characterized by N_2 adsorption/desorption isotherm measurements. The isotherm and pore size distribution curves are shown in Figure 5a,b. Three samples show type-II isotherms with hysteresis loops, suggesting the presence of the mesoporous structure. The specific surface areas of the 5% BN-G@MoS_2-10@90, 5% BN-G@MoS_2-50@50, and 5% BN-G@MoS_2-90@10 composite samples were 21.3, 36.9, and 68.2 m^2 g^{-1}, and the pore volume was 0.04, 0.09, and 0.11 cm^3 g^{-1}, respectively. The surface area of the 5% BN-G@MoS_2-90@10 (68.2 m^2 g^{-1}) composite is 3.2 times higher than that of 5% BN-G@MoS_2-10@90 (21.3 m^2 g^{-1}) and 1.84 times higher than that of the 5% BN-G@MoS_2-50@50 (36.9 m^2 g^{-1}) composite sample. The average pore size was 2.6 nm in all the samples. The surface area of the samples increased with increasing concentration of graphene. High specific surface area and high pore volume (mesoporous) provide additional active sites and expand the contact space between the electrolyte solution and electrode.

4.2. Electrochemical Characterization. First, by using CV and GCD measurements in an alkaline medium (6 M KOH), three electrodes were used to examine the electrochemical performance of 5% BN-G@MoS_2-50@50, 5% BN-G@MoS_2-10@90, and 5% BN-G@MoS_2-90@10. For this measurement, the potential window was for the compositions

https://doi.org/10.1021/acsomega.3c09877
ACS Omega 2024, 9, 15294−15303

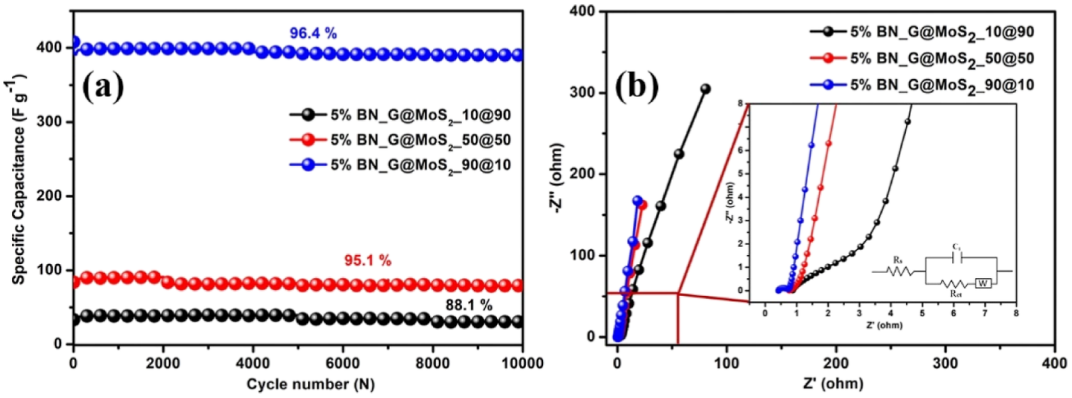

Figure 7. (a) Cycling stability at 1 A g^{-1} and (b) Nyquist plots before cycling and the fitted equivalent circuit of the 5% BN_G@MoS_2 nanocomposite (1:9, 5:5, and 9:1) electrodes.

in the voltage range of −0.4 to 0.6 V. The CV curves at different scan rates from 10 to 500 mV s^{-1} (Figure S4a−c) show the remarkable difference in electrochemical surface activity between 5% BN-G@MoS_2-50@50, 5% BN-G@MoS_2-10@90, and 5% BN-G@MoS_2-90@10 nanocomposites. For comparison, the curves of the three nanocomposites at a scan rate of 100 mV s^{-1} are shown in Figure 6a. All CV curves present a capacitive behavior with rectangular shapes and a hump in the CV curves, indicating electric double-layer capacitance (EDLC) behavior of graphene and the pseudocapacitance of MoS_2. However, the area and the current density response of 5% BN-G@MoS_2-90@10 are much higher than those of 5% BN-G@MoS_2-10@90 and 5% BN-G@MoS_2-50@50, indicating a higher specific capacitance value. To understand the state transitions during the cycling process and the reaction kinetics is needed to get additional insights into the remarkable electrochemical performance of BN-G@MoS_2 composites as a material for supercapacitors. As shown in Figure S4, we examined the CV curves of the BN-G@MoS_2 composites at different scan speeds. Usually expressed as $i = av^b$, the relationship between current (i) and scan rate (v) can be found using a log(i)−log (v) curve. Here, parts a and b are the variable constants. A complete diffusion-controlled process is indicated by b = 0.5, whereas b = 1 denotes a capacitive process fully responsible for charge storage. The results of the calculation indicate that the electrodes 5% h-BN_G@MoS_2_10@90, 5% h-BN_G@MoS_2_50@50, and 5% h-BN_G@MoS_2_90@10 exhibit a linear relationship between scan speed and peak current, as indicated by b = 0.84, 0.91, and 0.93 in Figure S5. This suggests that capacitance control, or surface drive, has a higher ratio of charge storage in comparison to diffusion control. In particular, because of the graphene proportion, 5% h-BN_G@MoS_2_90@10 exhibits a higher capacity contribution than diffusion.

The following formulas are used to determine the contribution from charge storage of the diffusive and capacitive types (eqs 4 and 5).

$$i(V) = k_1 v + k_2 v^{1/2} \tag{4}$$

$$\frac{i(V)}{v^{1/2}} = k_1 v^{1/2} + k_2 \tag{5}$$

where i is the current response at a scan rate of v and k_1 and k_2 are constants. The diffusive contribution is represented by $k_2 v^{1/2}$ and the capacitive contribution by $k_1 v$. It is possible to discern the percentage of capacitive and diffusion charge storage by looking at the plot of $\left(\frac{i(V)}{v^{1/2}}\right)$ and $v^{1/2}$ at a given potential (V) and finding the slope k_1 and Y-intercept k_2. Figure S6 shows the percentage contribution of the 5% h-BN_G@MoS_2_90@10 electrode at a potential of 0.2 V. The fraction of the capacitive contribution rises with an increase in scan rate.

The capacitive performance of the electrodes was further investigated with GCD measurements, as shown in Figure 6b. The comparatively symmetrical discharging curves compared to their charging counterparts further demonstrate the electrodes' excellent capacitive qualities. In accordance with the findings of the CV curves, the 5% BN-G@MoS_2-90@10 nanocomposite exhibits a higher charge/discharge curve at current densities of 1 A g^{-1} than the other two composites. The excellent reversibility of the nanocomposite is demonstrated by the charge curves of 5% BN-G@MoS_2-90@10 at different current densities from 1 to 20 A g^{-1}, which are almost symmetrical with their corresponding discharge counterparts, as shown in Figure 6c. Figures S7a and S8a present the GCD of 5% BN-G@MoS_2-50@50 and 5% BN-G@MoS_2-10@90. The specific capacitance values of the 5% BN-G@MoS_2-90@10, 5% BN-G@MoS_2-50@50, and 5% BN-G@MoS_2-10@90 nanocomposites were calculated at various current densities (1−20 A g^{-1}) with voltages between −0.4 and 0.6 V using eq 1 and are shown in Figures 6d, S7b, and S8b, respectively (Table S1). The specific capacitances of 5% BN-G@MoS_2-90@10, 5% BN-G@MoS_2-50@50, and 5% BN-G@MoS_2-10@90 nanocomposites at a current density of 1 A g^{-1} are 423, 83, and 38 F g^{-1}, respectively, which demonstrated that the electrochemical performance of 5% BN-G@MoS_2-90@10 has been improved dramatically due to the sufficient amount of graphene and uniform network structure, which has high contact with the electrolyte. At current densities of 1, 2, 3, 4, 5, 10, and 20 A g^{-1}, respectively, the specific capacitances of 5% BN-G@MoS_2-90@10 are 423, 349, 291, 273, 258, 198, and 162 F g^{-1}, where the minimum specific capacitance of 162 F g^{-1} at a current density of 20 A g^{-1} maintains 38% of the initial capacitance at a current density of 1 A g^{-1}. Due to the inability of the ions in the electrolyte to be quickly accessed and removed inside the electrode at high current densities, the electrode uses fewer electroactive species. Additionally, the effective interaction between the ions and the electrode could be gradually reduced with the continually rising current density based on the resistance and departure from the GCD curves that were seen. The cycle stability of the supercapacitor is

https://doi.org/10.1021/acsomega.3c09877
ACS Omega 2024, 9, 15294−15303

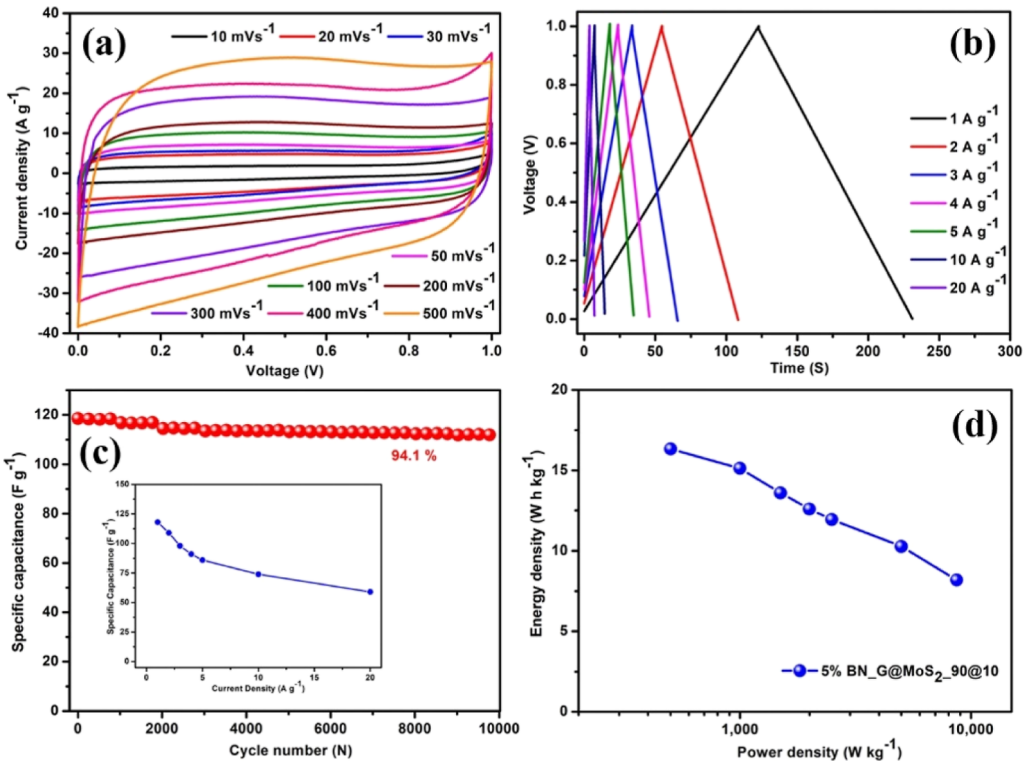

Figure 8. Electrochemical performance of symmetric supercapacitors measured in a two-electrode system. (a) CV curves at different scan rates from 10 to 500 mV s^{-1}; (b) GCD curves at different current densities from 1 to 20 A g^{-1}; (c) cycling stability measured at a current density of 1 A g^{-1} for 10,000 cycles; the inset shows the specific capacitances at different current densities from 1 to 20 A g^{-1}; and (d) Ragone plot related to energy density and power density.

crucial for the nanocomposites made of 5% BN-G@MoS_2-90@10, 5% BN-G@MoS_2-50@50, and 5% BN-G@MoS_2-10@90. It was tested using a galvanostatic charge and discharge study with a current density of 1 A g^{-1} in a solution of 6.0 M KOH for 10,000 cycles, as shown in Figure 7 a. The 5% BN-G@MoS_2-90@10, 5% BN-G@MoS_2-50@50, and 5% BN-G@MoS_2-10@90 nanocomposites exhibit good charge/discharge stability after 10,000 cycles, with capacity retentions of 96.4, 95.1, and 88.1%, respectively. The volume instability of MoS_2 under external current is the root cause of the poor cycling stability of 5% BN-G@MoS_2-50@50 and 5% BN-G@MoS_2-10@90 nanocomposites, which leads to the detachment of MoS_2 nanoparticles from the scaffold network. The specific capacitance conservation for the 5% BN-G@MoS_2-90@10 active material was 96.4%, showing good cycling life that can be due to the synergistic interaction between MoS_2, graphene, and h-BN as well as the practical ion diffusion channels created by KOH activation. These findings demonstrate the 5% BN-G@MoS_2-90@10 composite's capacity to meet the requirements of a long lifetime cycle and good rate capability, which are essential for usable energy storage devices.

One of the primary techniques for assessing the fundamental characteristics of electrode materials is EIS, which analyzes ion diffusion properties, internal resistance, and charge-transfer kinetics. EIS was conducted on the electrode materials 5% BN-G@MoS_2-90@10, 5% BN-G@MoS_2-50@50, and 5% BN-G@MoS_2-10@90 in the frequency range of 10 kHz−1 Hz before and after cycles in Figures 7b and S9. The depressed semicircle and the linear feature region in the high- and low-frequency regions of all materials, respectively, were clearly visible in the Nyquist plots. The intercepts on the *x*-axis displayed equivalent series resistance (R_s) matched with the internal resistance of the electrode active material, the electrolytic resistance, and the resistance at the interface between the current collector and the active material. The charge-transfer resistance (R_{ct}) and the high-frequency semicircle's diameter were compatible.[53] The R_s values of 5% BN-G@MoS_2-90@10, 5% BN-G@MoS_2-50@50, and 5% BN-G@MoS_2-10@90 before and after cycles are 0.42, 0.75, 0.86, and 0.45, 0.80, and 0.90 Ω, respectively. The R_{ct} values of the nanocomposite's electrodes before and after cycles are 0.72, 0.85, and 1.61 and 0.40, 0.91, and 2.85 Ω (Table S2), respectively, by the calculation with the Nyquist plots. We can find that both R_s and R_{ct} of 5% BN-G@MoS_2-90@10 are lower than those of 5% BN-G@MoS_2-50@50 and 5% BN-G@MoS_2-10@90, indicating that the electrical conductivity of MoS_2 has been improved after combination with the excellent conductive graphene. The adequate percentage of graphene in 5% BN-G@MoS_2-90@10 composition blocks the aggregation of MoS_2 nanoparticles and increases the efficient diffusion of electrolyte ions within the electrode.

Experiments were conducted by utilizing a two-electrode symmetric arrangement to assess the possible use of 5% BN-G@MoS_2-90@10 in electrochemical supercapacitors. As shown in Figure 8, the electrochemical performance was examined at room temperature. Figure 8 shows the CV profile of the as-prepared symmetric cell with a 5% BN-G@MoS_2-90@10 electrode at a potential range of 0−1.0 V in 6 M KOH electrolyte. The CV curves of the symmetric supercapacitor at different scan rates exhibit quasi rectangular shapes. The CV profile clearly shows that the 5% BN-G@MoS_2-90@10 electrode is stable at all scan rates and that EDLC, rather than pseudo capacitance, is the major source of capacitance. The GCD curves at various current densities (Figure 8 b)

https://doi.org/10.1021/acsomega.3c09877
ACS Omega 2024, 9, 15294−15303

show symmetrical triangle curves during charging and discharging in addition to good linear voltage/time profiles, illustrative of the device's exceptional capacitive performance and quick, reversible Faradaic reactions. The specific capacitances of the supercapacitor were calculated from its GCD curves, as shown in Figure 8c (inset). The supercapacitor delivered high capacitances of 118 F g^{-1} at a current density of 1 A g^{-1} and 59 F g^{-1} at a current density 20 A g^{-1} and maintains 50% of the initial capacitance at a current density 1 A g^{-1}. As shown in Figure 8c, the stability of the device was evaluated using the galvanostatic charge/discharge process at a current density of 1 A g^{-1}. After 10,000 cycles, the device still has roughly 94.1% of its initial capacitance. Graphene and h-BN are responsible for the material's exceptional electrochemical stability, which provides structural support during charging and discharging.

The energy and power densities of SCs are two crucial factors because they show how effectively they can be used as a power source. Equations 2 and 3 were used to get the associated energy density (E) and power density (P) based on GCD curves of various current densities, as illustrated in Figure 8d. 5% BN-G@MoS_2-90@10 device and those of available energy storage devices reported in the literature are compared in a Ragone diagram.[18,20,50,51,54−56] The synergistic effect of graphene, h-BN, and MoS_2 nanoparticles, where graphene serves as the conductive network, h-BN as the adhesion layer, and MoS_2 nanoparticles provide active sites for charge storage, may be responsible for the excellent electrochemical performance of the 5% BN-G@MoS_2-90@10 electrode. The maximum energy density of the 5% BN-G@MoS_2-90@10 supercapacitors is 16.33 W h/kg (power density is 501 W/kg), and the power density is 8671.76 W/kg.

5. CONCLUSIONS

In conclusion, 5% BN-G@MoS_2-90@10, 5% BN-G@MoS_2-50@50, and 5% BN-G@MoS_2-10@90 composites were prepared using the ball milling procedure and the precursor materials h-BN, MoS_2, and graphene. The supercapacitor's electrode material, 5% BN-G@MoS_2-90@10, has a high specific capacitance of 423 F g^{-1} at a current density of 1 A g^{-1} in 6 M KOH aqueous electrolyte and a capacitance retention of 96.4% after 10,000 cycles. A composite made of graphene and MoS_2 nanoparticles has outstanding cycling stability and rate capabilities. High specific capacitance (118 F g^{-1}), outstanding cycle performance (the capacity retains 94.1% after 10,000 cycles), and high energy and power densities are all advantages of the symmetric SC that was made with the 5% BN-G@MoS_2-90@10 composite. The synergistic interaction of MoS_2, graphene, and h-BN was said to be responsible for the superior electrochemical performances. According to the findings, the 5% BN-G@MoS_2-90@10 electrode has a wide range of potential applications in the field of energy storage devices.

ASSOCIATED CONTENT

Supporting Information

The Supporting Information is available free of charge at https://pubs.acs.org/doi/10.1021/acsomega.3c09877.

EDX mapping analysis, SEM image, and different percentages of atoms in the composite; HRTEM images; XPS spectra; CV profiles; log vs log(v) curves; separation of capacitance and diffusion capacity; GCD curves; Nyquist plots; specific capacitance; and variation of impedance (PDF)

AUTHOR INFORMATION

Corresponding Author

Edreese H. Alsharaeh − *College of Science and General Studies, AlFaisal University, Riyadh 11533, Saudi Arabia;* orcid.org/0000-0002-3707-7883; Email: ealsharaeh@alfaisal.edu

Authors

Chandra Sekhar Bongu − *College of Science and General Studies, AlFaisal University, Riyadh 11533, Saudi Arabia*

Muhammad Arsalan − *EXPEC Advanced Research Center, Saudi Aramco, Dhahran 31311, Saudi Arabia;* orcid.org/0000-0002-1502-8247

Complete contact information is available at: https://pubs.acs.org/10.1021/acsomega.3c09877

Notes

The authors declare no competing financial interest.

ACKNOWLEDGMENTS

This work is part of a research project PIF 726175. The authors gratefully acknowledge Alfaisal University and its Office of Research & innovation for their continuous support throughout this study.

REFERENCES

(1) Lu, X.; Yu, M.; Wang, G.; Tong, Y.; Li, Y. Flexible Solid-State Supercapacitors: Design, Fabrication and Applications. *Energy Environ. Sci.* **2014**, *7* (7), 2160−2181.

(2) Simon, P.; Gogotsi, Y.; Dunn, B. Where Do Batteries End and Supercapacitors Begin? *Science* **2014**, *343* (6176), 1210−1211.

(3) Kumar, K. S.; Choudhary, N.; Jung, Y.; Thomas, J. Recent Advances in Two-Dimensional Nanomaterials for Supercapacitor Electrode Applications. *ACS Energy Lett.* **2018**, *3* (2), 482−495.

(4) Wang, Y.; Song, Y.; Xia, Y. Electrochemical Capacitors: Mechanism, Materials, Systems, Characterization and Applications. *Chem. Soc. Rev.* **2016**, *45*, 5925−5950.

(5) Zhang, S.; Hu, R.; Dai, P.; Yu, X.; Ding, Z.; Wu, M.; Li, G.; Ma, Y.; Tu, C. Synthesis of Rambutan-like MoS2/Mesoporous Carbon Spheres Nanocomposites with Excellent Performance for Supercapacitors. *Appl. Surf. Sci.* **2017**, *396*, 994−999.

(6) Sahoo, S.; Pazhamalai, P.; Krishnamoorthy, K.; Kim, S.-J. Hydrothermally Prepared α-MnSe Nanoparticles as a New Pseudocapacitive Electrode Material for Supercapacitor. *Electrochim. Acta* **2018**, *268*, 403−410.

(7) Deng, Z.; Hu, Y.; Ren, D.; Lin, S.; Jiang, H.; Li, C. Reciprocal Hybridization of MoO 2 Nanoparticles and Few-Layer MoS 2 for Stable Lithium-Ion Batteries. *Chem. Commun.* **2015**, *51* (72), 13838−13841.

(8) Candelaria, S. L.; Shao, Y.; Zhou, W.; Li, X.; Xiao, J.; Zhang, J.-G.; Wang, Y.; Liu, J.; Li, J.; Cao, G. Nanostructured Carbon for Energy Storage and Conversion. *Nano energy* **2012**, *1* (2), 195−220.

(9) Shinde, S. S.; Gund, G. S.; Kumbhar, V. S.; Patil, B. H.; Lokhande, C. D. Novel Chemical Synthesis of Polypyrrole Thin Film Electrodes for Supercapacitor Application. *Eur. Polym. J.* **2013**, *49* (11), 3734−3739.

(10) Jia, R.; Li, L.; Ai, Y.; Du, H.; Zhang, X.; Chen, Z.; Shen, G. Self-Healable Wire-Shaped Supercapacitors with Two Twisted NiCo 2 O 4 Coated Polyvinyl Alcohol Hydrogel Fibers. *Sci. China Mater.* **2018**, *61* (2), 254−262.

(11) Kannan, P. K.; Late, D. J.; Morgan, H.; Rout, C. S. Recent Developments in 2D Layered Inorganic Nanomaterials for Sensing. *Nanoscale* **2015**, *7* (32), 13293−13312.

(12) Peng, Q.; De, S. Outstanding Mechanical Properties of Monolayer MoS 2 and Its Application in Elastic Energy Storage. *Phys. Chem. Chem. Phys.* **2013**, *15* (44), 19427−19437.
(13) Yu, X. Y.; David Lou, X. W. Mixed Metal Sulfides for Electrochemical Energy Storage and Conversion. *Adv. Energy Mater.* **2018**, *8* (3), 1701592.
(14) Yu, X.; Yu, L.; Lou, X. W. Metal Sulfide Hollow Nanostructures for Electrochemical Energy Storage. *Adv. Energy Mater.* **2016**, *6* (3), 1501333.
(15) da Silveira Firmiano, E. G.; Rabelo, A. C.; Dalmaschio, C. J.; Pinheiro, A. N.; Pereira, E. C.; Schreiner, W. H.; Leite, E. R. Supercapacitor Electrodes Obtained by Directly Bonding 2D MoS2 on Reduced Graphene Oxide. *Adv. Energy Mater.* **2014**, *4* (6), 1301380.
(16) Tang, H.; Wang, J.; Yin, H.; Zhao, H.; Wang, D.; Tang, Z. Growth of Polypyrrole Ultrathin Films on MoS2Monolayers as High-performance Supercapacitor Electrodes. *Adv. Mater.* **2015**, *27* (6), 1117−1123.
(17) Ji, H.; Liu, C.; Wang, T.; Chen, J.; Mao, Z.; Zhao, J.; Hou, W.; Yang, G. Porous Hybrid Composites of Few-layer MoS2 Nanosheets Embedded in a Carbon Matrix with an Excellent Supercapacitor Electrode Performance. *Small* **2015**, *11* (48), 6480−6490.
(18) Gupta, H.; Chakrabarti, S.; Mothkuri, S.; Padya, B.; Rao, T. N.; Jain, P. K. High Performance Supercapacitor Based on 2D-MoS2 Nanostructures. *Mater. Today: Proc.* **2020**, *26*, 20−24.
(19) Wang, Y.; Chou, S.; Wexler, D.; Liu, H.; Dou, S. High-Performance Sodium-Ion Batteries and Sodium-Ion Pseudocapacitors Based on MoS2/Graphene Composites. *Chem. - Eur. J.* **2014**, *20* (31), 9607−9612.
(20) Bao, J.; Zeng, X.-F.; Huang, X.-J.; Chen, R.-K.; Wang, J.-X.; Zhang, L.-L.; Chen, J.-F. Three-Dimensional MoS2/rGO Nanocomposites with Homogeneous Network Structure for Supercapacitor Electrodes. *J. Mater. Sci.* **2019**, *54* (24), 14845−14858.
(21) Huang, K.-J.; Zhang, J.-Z.; Shi, G.-W.; Liu, Y.-M. Hydrothermal Synthesis of Molybdenum Disulfide Nanosheets as Supercapacitors Electrode Material. *Electrochim. Acta* **2014**, *132*, 397−403.
(22) Wang, X.; Ding, J.; Yao, S.; Wu, X.; Feng, Q.; Wang, Z.; Geng, B. High Supercapacitor and Adsorption Behaviors of Flower-like MoS 2 Nanostructures. *J. Mater. Chem. A* **2014**, *2* (38), 15958−15963.
(23) Saraf, M.; Natarajan, K.; Saini, A. K.; Mobin, S. M. Small Biomolecule Sensors Based on an Innovative MoS 2-rGO Heterostructure Modified Electrode Platform: A Binder-Free Approach. *Dalton Trans.* **2017**, *46* (45), 15848−15858.
(24) Yang, M.; Ko, S.; Im, J. S.; Choi, B. G. Free-Standing Molybdenum Disulfide/Graphene Composite Paper as a Binder-and Carbon-Free Anode for Lithium-Ion Batteries. *J. Power Sources* **2015**, *288*, 76−81.
(25) Guo, Y.; Qi, X.; Fu, X.; Hu, Y.; Peng, Z. Vertically Standing Ultrathin MoS2 Nanosheet Arrays on Molybdenum Foil as Binder-Free Anode for Lithium-Ion Batteries. *J. Mater. Sci.* **2019**, *54* (5), 4105−4114.
(26) Zhou, J.; Qin, J.; Zhao, N.; Shi, C.; Liu, E.-Z.; He, F.; Li, J.; He, C. Salt-Template-Assisted Synthesis of Robust 3D Honeycomb-like Structured MoS 2 and Its Application as a Lithium-Ion Battery Anode. *J. Mater. Chem. A* **2016**, *4* (22), 8734−8741.
(27) Xie, D.; Tang, W.; Xia, X.; Wang, D.; Zhou, D.; Shi, F.; Wang, X.; Gu, C.; Tu, J. Integrated 3D Porous C-MoS2/Nitrogen-Doped Graphene Electrode for High Capacity and Prolonged Stability Lithium Storage. *J. Power Sources* **2015**, *296*, 392−399.
(28) Ren, L.; Zhang, G.; Yan, Z.; Kang, L.; Xu, H.; Shi, F.; Lei, Z.; Liu, Z.-H. Three-Dimensional Tubular MoS2/PANI Hybrid Electrode for High Rate Performance Supercapacitor. *ACS Appl. Mater. Interfaces* **2015**, *7* (51), 28294−28302.
(29) Yang, T.; Yang, R.; Chen, H.; Nan, F.; Ge, T.; Jiao, K. Electrocatalytic Activity of Molybdenum Disulfide Nanosheets Enhanced by Self-Doped Polyaniline for Highly Sensitive and Synergistic Determination of Adenine and Guanine. *ACS Appl. Mater. Interfaces* **2015**, *7* (4), 2867−2872.
(30) Wang, Y.; Yu, L.; Lou, X. W. Formation of Triple-shelled Molybdenum-Polydopamine Hollow Spheres and Their Conversion into MoO2/Carbon Composite Hollow Spheres for Lithium-ion Batteries. *Angew. Chem., Int. Ed.* **2016**, *55* (47), 14668−14672.
(31) Shang, P.; Zhang, J.; Tang, W.; Xu, Q.; Guo, S. 2D Thin Nanoflakes Assembled on Mesoporous Carbon Nanorods for Enhancing Electrocatalysis and for Improving Asymmetric Supercapacitors. *Adv. Funct. Mater.* **2016**, *26* (43), 7766−7774.
(32) Ekspong, J.; Sharifi, T.; Shchukarev, A.; Klechikov, A.; Wågberg, T.; Gracia-Espino, E. Stabilizing Active Edge Sites in Semicrystalline Molybdenum Sulfide by Anchorage on Nitrogen-doped Carbon Nanotubes for Hydrogen Evolution Reaction. *Adv. Funct. Mater.* **2016**, *26* (37), 6766−6776.
(33) Zhang, F.; Tang, Y.; Liu, H.; Ji, H.; Jiang, C.; Zhang, J.; Zhang, X.; Lee, C.-S. Uniform Incorporation of Flocculent Molybdenum Disulfide Nanostructure into Three-Dimensional Porous Graphene as an Anode for High-Performance Lithium Ion Batteries and Hybrid Supercapacitors. *ACS Appl. Mater. Interfaces* **2016**, *8* (7), 4691−4699.
(34) Zhang, L.; Lou, X. W. Hierarchical MoS2 Shells Supported on Carbon Spheres for Highly Reversible Lithium Storage. *Chem. - Eur. J.* **2014**, *20* (18), 5219−5223.
(35) Huang, Y.; Liang, J.; Chen, Y. An Overview of the Applications of Graphene-based Materials in Supercapacitors. *Small* **2012**, *8* (12), 1805−1834.
(36) Yang, X.; Cheng, C.; Wang, Y.; Qiu, L.; Li, D. Liquid-Mediated Dense Integration of Graphene Materials for Compact Capacitive Energy Storage. *Science* **2013**, *341* (6145), 534−537.
(37) Bai, Y.; Rakhi, R.; Chen, W.; Alshareef, H. N. Effect of pH-Induced Chemical Modification of Hydrothermally Reduced Graphene Oxide on Supercapacitor Performance. *J. Power Sources* **2013**, *233*, 313−319.
(38) Choi, H.-J.; Jung, S.-M.; Seo, J.-M.; Chang, D. W.; Dai, L.; Baek, J.-B. Graphene for Energy Conversion and Storage in Fuel Cells and Supercapacitors. *Nano Energy* **2012**, *1* (4), 534−551.
(39) He, P.; Zhao, K.; Huang, B.; Zhang, B.; Huang, Q.; Chen, T.; Zhang, Q. Mechanically Robust and Size-Controlled MoS2/Graphene Hybrid Aerogels as High-Performance Anodes for Lithium-Ion Batteries. *J. Mater. Sci.* **2018**, *53* (6), 4482−4493.
(40) Dutta, S.; De, S. MoS2 Nanosheet/rGO Hybrid: An Electrode Material for High Performance Thin Film Supercapacitor. *Mater. Today: Proc.* **2018**, *5* (3), 9771−9775.
(41) Luo, W.; Zhou, L.; Fu, K.; Yang, Z.; Wan, J.; Manno, M.; Yao, Y.; Zhu, H.; Yang, B.; Hu, L. A Thermally Conductive Separator for Stable Li Metal Anodes. *Nano Lett.* **2015**, *15* (9), 6149−6154.
(42) Angizi, S.; Alem, S. A. A.; Pakdel, A. Towards Integration of Two-Dimensional Hexagonal Boron Nitride (2D h-BN) in Energy Conversion and Storage Devices. *Energies* **2022**, *15* (3), 1162.
(43) Zhang, K.; Feng, Y.; Wang, F.; Yang, Z.; Wang, J. Two Dimensional Hexagonal Boron Nitride (2D-hBN): Synthesis, Properties and Applications. *J. Mater. Chem. C* **2017**, *5* (46), 11992−12022.
(44) Rodrigues, M. F.; Kalaga, K.; Gullapalli, H.; Babu, G.; Reddy, A. L. M.; Ajayan, P. M. Hexagonal Boron Nitride-Based Electrolyte Composite for Li-Ion Battery Operation from Room Temperature to 150 °C. *Adv. Energy Mater.* **2016**, *6* (12), 1600218.
(45) Arora, P.; Zhang, Z. Battery Separators. *Chem. Rev.* **2004**, *104* (10), 4419−4462.
(46) Zhang, X.; Ji, L.; Toprakci, O.; Liang, Y.; Alcoutlabi, M. Electrospun Nanofiber-Based Anodes, Cathodes, and Separators for Advanced Lithium-Ion Batteries. *Polym. Rev.* **2011**, *51* (3), 239−264.
(47) Wu, H.; Zhuo, D.; Kong, D.; Cui, Y. Improving Battery Safety by Early Detection of Internal Shorting with a Bifunctional Separator. *Nat. Commun.* **2014**, *5* (1), 5193.
(48) Wang, C.; Wan, W.; Huang, Y.; Chen, J.; Zhou, H. H.; Zhang, X. X. Hierarchical MoS 2 Nanosheet/Active Carbon Fiber Cloth as a Binder-Free and Free-Standing Anode for Lithium-Ion Batteries. *Nanoscale* **2014**, *6* (10), 5351−5358.
(49) Bindumadhavan, K.; Srivastava, S. K.; Mahanty, S. MoS 2-MWCNT Hybrids as a Superior Anode in Lithium-Ion Batteries. *Chem. Commun.* **2013**, *49* (18), 1823−1825.

https://doi.org/10.1021/acsomega.3c09877
ACS Omega 2024, 9, 15294−15303

(50) Thakur, A. K.; Majumder, M.; Choudhary, R. B.; Singh, S. B. MoS2 Flakes Integrated with Boron and Nitrogen-Doped Carbon: Striking Gravimetric and Volumetric Capacitive Performance for Supercapacitor Applications. *J. Power Sources* **2018**, *402*, 163−173.
(51) Li, X.; Zhang, C.; Xin, S.; Yang, Z.; Li, Y.; Zhang, D.; Yao, P. Facile Synthesis of MoS2/Reduced Graphene Oxide@ Polyaniline for High-Performance Supercapacitors. *ACS Appl. Mater. Interfaces* **2016**, *8* (33), 21373−21380.
(52) Ling, X.; Lin, Y.; Ma, Q.; Wang, Z.; Song, Y.; Yu, L.; Huang, S.; Fang, W.; Zhang, X.; Hsu, A. L. Parallel Stitching of Two-Dimensional Materials. *arXiv* **2015**, arXiv:1512.04492. preprint
(53) Li, X.; Yang, Z.; Qi, W.; Li, Y.; Wu, Y.; Zhou, S.; Huang, S.; Wei, J.; Li, H.; Yao, P. Binder-Free Co3O4@ NiCoAl-Layered Double Hydroxide Core-Shell Hybrid Architectural Nanowire Arrays with Enhanced Electrochemical Performance. *Appl. Surf. Sci.* **2016**, *363*, 381−388.
(54) Palsaniya, S.; Nemade, H. B.; Dasmahapatra, A. K. Synthesis of Polyaniline/Graphene/MoS2 Nanocomposite for High Performance Supercapacitor Electrode. *Polymer* **2018**, *150*, 150−158.
(55) Zhao, C.; Zhou, Y.; Ge, Z.; Zhao, C.; Qian, X. Facile Construction of MoS2/RCF Electrode for High-Performance Supercapacitor. *Carbon* **2018**, *127*, 699−706.
(56) Liu, J.; Khanam, Z.; Ahmed, S.; Wang, T.; Wang, H.; Song, S. Flexible Antifreeze Zn-Ion Hybrid Supercapacitor Based on Gel Electrolyte with Graphene Electrodes. *ACS Appl. Mater. Interfaces* **2021**, *13* (14), 16454−16468.

https://doi.org/10.1021/acsomega.3c09877
ACS Omega 2024, 9, 15294−15303